AIChE

Direct Numerical Simulations of Aggregation of Monosized Spherical Particles in Homogeneous Isotropic Turbulence

J. J. Derksen
Chemical and Materials Engineering, University of Alberta, Edmonton, Alberta, T6G 2G6 Canada

DOI 10.1002/aic.12761
Published online October 21, 2011 in Wiley Online Library (wileyonlinelibrary.com).

Direct numerical simulations of turbulent solid–liquid suspensions have been performed. The liquid is Newtonian, and the particles are identical spheres. The spheres have a tendency to aggregate since they are attracted to one another as a result of a square-well potential. The size of the particles is typically larger than the Kolmogorov scale, albeit of the same order of magnitude. In such situations, the particle dynamics (including the aggregation process), and turbulence strongly interact which explains the need for direct simulations. The lattice-Boltzmann method combined with an immersed boundary method for representing the no-slip conditions at the spherical solid–liquid interfaces was used. The results show that the aggregate size distributions depend on both the strength of particle–particle interactions and the intensity of the turbulence. © 2011 American Institute of Chemical Engineers *AIChE J,* 58: 2589–2600, 2012
Keywords: solid–liquid flow, turbulence, aggregation, lattice-Boltzmann method, square-well potential

Introduction

In many processes involving solid particle formation or solids handling, particles have a tendency to stick together. In crystallization processes crystals tend to agglomerate if they are in a supersaturated environment.[1,2] Suspension polymerization processes go through a ''sticky-phase'' with significant levels of aggregation.[3] In colloidal science, stabilization of colloids (e.g., based on extending electrostatic double-layers) is important, otherwise Van der Waals interactions would induce aggregation.[4] Promoting flocculation is employed in minerals and mining applications to enhance settling rates in gravity based separations.[5] Previously we used terms like aggregation, agglomeration and flocculation. In addition, cluster formation[6] and coagulation[7] are used to describe similar phenomena. In the rest of this article the (more generic) term *aggregation* has been used.

Sometimes aggregation is a wanted phenomenon to effectively grow particles for, e.g., making separation easier. It also is a mechanism that potentially destroys a narrow particle-size distribution, and as a result could deteriorate product quality. Much effort goes into preventing or promoting aggregation, and much effort goes into repairing the harm aggregation has done (e.g., in grinding and milling process steps[8]). Regardless if aggregation is wanted or unwanted, it is relevant to study the physical mechanisms underlying aggregation for better control of processes and for better process design. Given the multiscale character of many industrial processes in general and solids-handling processes in particular, there is a multitude of length and time scales that needs to be considered. They range from the molecular level of the microscopic mechanisms responsible for interaction forces, to the size of the process equipment that is designed to bring about transport processes (heat and mass transfer), in many cases by generating a turbulent hydrodynamic environment.

In this article, the focus is on the hydrodynamics related to aggregation. With the solids suspended in a fluid phase, hydrodynamics interact in various ways with aggregation processes. The deformations in the fluid phase and associated velocity gradients promote particle–particle collisions. Dependent sometimes on very intricate details (relative velocities before the collision, strength of the interparticle forces, relative orientation of particles, the hydrodynamic and/or chemical environment surrounding the colliding particles) collision events lead to aggregation events. Next to fluid-shear-induced (orthokinetic) aggregation, Brownian motion causes collisions and so-called perikinetic aggregation. In polydisperse systems different settling rates of different types of particles make them collide. In this article, the primary particles are assumed to be sufficiently large not to undergo Brownian motion, and Brownian motion will not be considered as a collision and aggregation mechanism. Also net gravity is discarded as a source of aggregation: we assume strongly turbulent flow and monodisperse primary particles.

The same fluid deformations that promote collisions and aggregation are also responsible for breakage of aggregates due to the mechanical stresses they exert on them. In turbulent flow, the hydrodynamic environment seen by an aggregate largely depends on its size relative to the hydrodynamic microscales (the Kolmogorov scale). For aggregates much smaller than the Kolmogorov scale the surrounding flow has a simple homogeneous structure that can be captured by a single deformation tensor that continuously changes when traveling with an aggregate through the turbulent flow. If the aggregates have a size comparable to or larger than the

Correspondence concerning this article should be addressed to J. J. Derksen at jos@ualberta.ca.

Kolmogorov scale, their hydrodynamic environment gets inhomogeneous and, therefore, more complex.

A large portion of the literature on aggregation modeling deals with population balance equations (PBE's) and efficient ways to solve them. PBE's are systems of equations that keep track of aggregate size distributions (ASD's) as a function of time (and sometimes location) by considering breakage, aggregation, and transport in physical and property space. The latter includes growth and dissolution of aggregates as a result of mass transfer with their environment.[9] Advances in the field of PBE's relate to solution strategies, such as methods based on the moments of ASD's[10] and the method of characteristics,[11] and on the identification of the mathematical structure of aggregation and breakage terms that allow for ASD's to reach a dynamic equilibrium.[12] The predictive power of PBE solutions critically depends on the level of realism and detail contained in the breakage and aggregation terms, including their dependence on the flow physics.

In the context of population balances, the physical descriptions of breakage due to flow[13,14] date back quite some time and are based on very simple notions of the flow field surrounding aggregates.[15,16] These notions are prone to refinement in terms of a better representation of the hydrodynamic environment, and in terms of improving estimates of the actual hydrodynamic forces in aggregates immersed in complex flow.[17]

In more recent literature, some of the aforementioned issues identified prompted very detailed modeling of aggregates in homogeneous deformation fields.[7,18–23] The—in such cases—small size of the aggregates compared to the fluid dynamic microscales allows for a Stokes flow approximation at the particle level and, thus, for the use of, e.g., Stokesian dynamics[24] to describe the interactions between the primary particles (spheres in case of Stokesian dynamics) forming aggregates, and the surrounding fluid. In such simulations, the overall deformation field that agitates the Stokesian dynamics is an input condition. It is, for instance, generated by means of computational fluid dynamics at the larger scales[23] or represents a canonical flow such as simple shear[25] or purely extensional flow. This essentially assumes a one-way coupling between the imposed flow at the larger scale and the flow at the length scales of the aggregate: the flow imposed on the aggregate generates deformation, breakage, and clustering events that have impact on the flow directly surrounding the aggregate. These effects are, however, not fed back to the imposed flow. This is a fair assumption given the wide separation of the turbulent microscale (represented by the imposed flow) and the scale of the (much smaller) aggregates.

In this article, we remove the assumption of aggregates being small compared to the Kolmogorov scale. This has a few consequences. In the first place it implies that Reynolds numbers based on aggregate size and even on primary particle size (the latter defined as $\mathrm{Re} = \frac{a^2\dot{\gamma}}{\nu}$ with $\dot{\gamma}$ the magnitude of the deformation rate tensor, a the primary particle radius, and ν the kinematic viscosity of the liquid) are not necessarily (much) smaller than unity and that inertial effects (of fluid as well as of the particles) need to be resolved (and Stokesian dynamics can not be applied). It also implies that there is no clear length-scale distinction between Kolmogorov-scale flow and aggregate-scale flow anymore. Both scales overlap in an order-of-magnitude sense and directly interact. Therefore, a direct, two-way coupling between the turbulent microscales and the inhomogeneous fluid deformation experienced by, and generated by the moving, rotating, and continuously restructuring aggregates needs to be established.

In our simulations, homogeneous, isotropic turbulence (HIT) is generated in a cubic, fully periodic, three-dimensional (3-D) domain through linear forcing.[26] Linear forcing is a computationally efficient way to establish HIT with a preset overall power input. In linear forcing, the turbulence is driven by a body force that is proportional to the local fluid velocity with a proportionality constant that is a function of (overall) power input and turbulent kinetic energy. With linear forcing we have control over the energy dissipation rate (and, thus, the Kolmogorov length scale) once stationary conditions are reached and dissipation balances power input. In the turbulent field, uniformly sized, spherical primary solid particles are released. The solids typically occupy 10% of the total volume. In the simulations the solid particles have finite size, and the solid–liquid interfaces are resolved, that is, a no slip condition is imposed at the surfaces of the moving (translating and rotating) spheres.

The particles are made sticky (i.e., they have a tendency to aggregate) by means of a square-well potential defined by a distance of interaction δ, and a binding energy E_{swp}.[27] If the centers of two approaching spheres come within a distance $2(a + \delta)$ they exchange potential energy for kinetic energy (by an amount E_{swp} per sphere). They then are within one another's square-well potential (SqWP) and are considered attached. Two attached spheres can only separate if they are able to overcome the potential energy barrier imposed by the SqWP with their kinetic energy (see the subsequent section for a more detailed description). The parameters E_{swp} and δ can, thus, be interpreted as the depth and the width of the square well, respectively. Next to interacting through the SqWP, the particles interact via the interstitial fluid and through hard-sphere collisions. The combination of turbulence and the SqWP produces a solid–liquid system in which bonds between primary spheres are continuously formed and broken, and an ASD evolves naturally to a dynamically stationary state. Our main interest is how the ASD depends on turbulence properties on one side, and the interaction potential on the other.

The simulations are based on the lattice-Boltzmann method for simulating fluid flow. The method and its applications have been discussed in review articles (e.g., by Chen and Doolen[28]), and the monograph by Succi.[29] The no-slip conditions at the moving sphere surfaces are imposed through an immersed boundary method.[30,31] By applying the immersed boundary method on each sphere surface we resolve the solid–liquid interfaces and the hydrodynamic force and torque acting on each sphere. The latter we use to update their linear and rotational equations of motion. This directly couples the solids and fluid phase, and fully accounts for the finite size of the particles.

The article is organized as follows: we first define the flow systems in terms of a set of dimensionless numbers that span our physical parameter space. We then discuss the numerical procedure and the modeling choices we made. The numerical procedure adds to the parameter space, the most important parameter being the (finite) size of our flow systems (relative to the particle size). When presenting the results in the subsequent section first a few verification tests

for the implementation of the SqWP (which is a novel part in our computational procedure) are described. Then we show results for aggregation in homogeneous, isotropic turbulence with emphasis on aggregate size distributions and aggregate fractal dimensions as a function of flow and particle properties. A summary and conclusions are given at the end of the article.

Flow Systems

We consider fully periodic, cubic, 3-D domains of L^3 volume that contain incompressible Newtonian fluid with density ρ, and kinematic viscosity ν, and uniformly sized solid spherical particles with radius a and density ρ_p. The solids volume fraction ϕ is in the range 0.04 to 0.16; the aspect ratio $\frac{L}{a}$ in the range 21.3 to 64. Given the solid–liquid systems we are interested in, the density ratio $\frac{\rho_p}{\rho}$ has been set to a fixed value of 4.0.

In the flow domain we create homogeneous, isotropic turbulence through linear forcing.[26] In linear forcing a body force $\mathbf{g}$ (force per unit mass) that is proportional to the local fluid velocity acts on the fluid $\mathbf{g} = A\mathbf{u}$: with the proportionality factor $A = \frac{\varepsilon}{3u_{rms}^2}$, ε the volume-averaged energy dissipation rate, and u_{rms} the volume-averaged root-mean-square fluid velocity. One way to operate linear forcing is to set ε to a constant value (in space and time), and to determine A each time step by updating u_{rms} each time step based on spatial averaging of the actual flow field. This allows us to control the turbulence in terms of its energy dissipation rate and, therefore, in terms of its Kolmogorov length-scale $\eta_K = \left(\frac{\nu^3}{\varepsilon}\right)^{1/4}$. In this way the ratio of Kolmogorov length scale over primary particle size $\frac{\eta_K}{a}$ is a dimensionless input parameter to the simulations. As discussed in the Introduction, flow systems with ratios $\frac{\eta_K}{a}$ smaller than unity have been simulated.

Simulations involving resolved (finite-size) particles in HIT in periodic cubic domains have been reported earlier.[32,33] In Ref. 33 the particles are released in a decaying (nonforced) turbulent flow. In this article, the turbulence needs to be sustained and, thus, forced given the relatively long time scales of the aggregation process and our desire to predict stationary ASD's. For this we need a sufficiently long time window with steady conditions for collecting meaningful ASD's and flow statistics.

The spheres interact via a square-well potential[27] that serves as the model mechanism for aggregation. If two spheres (i and j) approach one another and reach a center-to-center distance of $2(a + \delta)$, they enter the square well and are considered "attached". At that moment an attraction potential kicks in that induces a stepwise change in the velocities of spheres i and j, i.e., an amount J is instantaneously added to the relative radial approach velocity of the two spheres

$$\tilde{\mathbf{u}}_{\mathbf{pi}} = \mathbf{u}_{\mathbf{pi}} + \frac{1}{2}J\mathbf{n}, \quad \tilde{\mathbf{u}}_{\mathbf{pj}} = \mathbf{u}_{\mathbf{pj}} - \frac{1}{2}J\mathbf{n} \tag{1}$$

with $\mathbf{u}_{\mathbf{pi}}$, $\mathbf{u}_{\mathbf{pj}}$ pre-entry sphere velocities, and $\tilde{\mathbf{u}}_{\mathbf{pi}}$, $\tilde{\mathbf{u}}_{\mathbf{pj}}$ post-entry velocities, and $J = \sqrt{\left(\Delta\mathbf{u}_{\mathbf{ij}} \cdot \mathbf{n}\right)^2 + (2\Delta u)^2} + \Delta\mathbf{u}_{\mathbf{ij}} \cdot \mathbf{n}$. The unit vector $\mathbf{n}$ points from the center of sphere i to the center of sphere j, $\Delta\mathbf{u}_{\mathbf{ij}} \equiv \mathbf{u}_{\mathbf{pj}} - \mathbf{u}_{\mathbf{pi}}$, and Δu is the parameter defining the strength of the SqWP (see below). Note that for two approaching spheres $\Delta\mathbf{u}_{\mathbf{ij}} \cdot \mathbf{n} < 0$, and, thus $J = 0$ if $\Delta u = 0$ (i.e., a zero-strength SqWP).

In energy terms this means that on entering the square well, potential energy is converted in kinetic energy by total amount $2E_{swp} = 2\left(\frac{1}{2}m_p(\Delta u)^2\right)$ (with $m_p = \frac{4}{3}\pi\rho_p a^3$ the mass of one sphere). Since there are two spheres involved in the process, on average each sphere gains E_{swp} kinetic energy. Once in each other's square well the spheres keep moving under the influence of hydrodynamic forces and possibly undergo hard-sphere collisions according to the two-parameter model (restitution coefficient e and friction coefficient μ) due to[34]: In a hard-sphere collision, two particles i and j having precollision linear and angular velocity $\mathbf{u}_{\mathbf{pi}}$, $\mathbf{u}_{\mathbf{pj}}$, $\boldsymbol{\omega}_{\mathbf{pi}}$, and $\boldsymbol{\omega}_{\mathbf{pj}}$ exchange momentum according to

$$\hat{\mathbf{u}}_{\mathbf{pi}} = \mathbf{u}_{\mathbf{pi}} + \mathbf{Q}, \quad \hat{\mathbf{u}}_{\mathbf{pj}} = \mathbf{u}_{\mathbf{pj}} - \mathbf{Q}, \quad \hat{\boldsymbol{\omega}}_{\mathbf{pi}} = \boldsymbol{\omega}_{\mathbf{pi}} + \frac{5}{2a}\mathbf{n} \times \mathbf{Q}, \quad \hat{\boldsymbol{\omega}}_{\mathbf{pj}} = \boldsymbol{\omega}_{\mathbf{pj}} + \frac{5}{2a}\mathbf{n} \times \mathbf{Q} \tag{2}$$

The superscript $\hat{}$ indicates post-collision quantities, and (as before) $\mathbf{n}$ is the unit vector pointing from the center of sphere i to the center of sphere j. The momentum exchange vector $\mathbf{Q}$ can be decomposed in a normal and tangential part $\mathbf{Q} = Q_n\mathbf{n} + Q_t\mathbf{t}$. The tangential unit vector $\mathbf{t}$ is in the direction of the precollision slip velocity $\mathbf{c}_\mathbf{c}$ between the sphere surfaces at the point of contact

$$\mathbf{c}_\mathbf{c} = \Delta\mathbf{u}_{\mathbf{ij}} - [\Delta\mathbf{u}_{\mathbf{ij}} \cdot \mathbf{n}]\mathbf{n} - a\boldsymbol{\omega}_{\mathbf{pi}} \times \mathbf{n} - a\boldsymbol{\omega}_{\mathbf{pj}} \times \mathbf{n}. \tag{3}$$

In the collision model[34] the components of the momentum exchange vector are

$$Q_n = \frac{(1+e)}{2}\Delta\mathbf{u}_{\mathbf{ij}} \cdot \mathbf{n}, \quad Q_t = \min\left[-\mu Q_n, \frac{1}{7}|\mathbf{c}_\mathbf{c}|\right] \tag{4}$$

As indicated in the expression for Q_t (Eq. 4), the collision switches between a slipping and a sticking collision at $-\mu Q_n = \frac{1}{7}|\mathbf{c}_\mathbf{c}|$. In some simulations the friction coefficient μ was set to infinity which means that in such a simulation a collision always is a sticking collision (with $Q_t = \frac{1}{7}|\mathbf{c}_\mathbf{c}|$).

If two attached spheres move apart and reach a center-to-center distance of $2(a + \delta)$ they need sufficient kinetic energy to escape the SqWP: they need a relative radial separation velocity $\Delta\mathbf{u}_{\mathbf{ij}} \cdot \mathbf{n}$ (upon separation this inner product is positive) of at least $2\Delta u$. If they are able to escape, kinetic energy is converted back to potential energy upon escaping. If they are not able to escape they reverse their relative radial velocity at the moment they reach the edge of the square well and stay attached. The square-well potential is, thus, defined by two parameters: its width δ and its energy E_{swp}. Rather than working with the energy, we will be working with Δu in the remainder of this article. As indicated, the two are related according to $E_{swp} = \frac{1}{2}m_p(\Delta u)^2$.

This leaves us with four parameters governing direct (as opposed to hydrodynamic) particle–particle interactions. In terms of dimensionless numbers these are the collision parameters e and μ, and the square-well potential parameters $\frac{\delta}{a}$, and $\frac{\Delta u}{\upsilon}$ with $\upsilon = (\nu\varepsilon)^{1/4}$ the Kolmogorov velocity scale. In our study we keep the restitution coefficient constant and equal to $e = 1.0$. The rationale for this is that for liquid–solid systems

most of the energy dissipation takes place in the liquid, not so much in the solid-solid contacts.[35]

To summarize the input parameter space in terms of dimensionless numbers, they are the solids volume fraction ϕ, the domain size over sphere radius $\frac{L}{a}$, the solid over liquid density ratio $\frac{\rho_p}{\rho}$, the ratio of Kolmogorov length scale over particle radius $\frac{\eta_K}{a}$, the dimensionless width and depth of the square well $\frac{\delta}{a}$ and $\frac{\Delta u}{v}$, and the restitution coefficient e, and the friction coefficient μ. The solid–liquid systems discussed in this article only cover part of the parameter space. The fixed parameters are $\frac{\rho_p}{\rho} = 4.0$, $e = 1.0$, and $\frac{\delta}{a} = 0.05$. For the friction coefficient we have taken two extreme values $\mu = 0$ and $\mu \to \infty$, i.e., perfectly smooth (frictionless) collisions, and collisions where the particles exchange tangential momentum such that after the collisions the tangential velocity at the point of contact is the same for the two spheres involved in the collision. The impact of the remainder of the dimensionless parameters on the aggregation process has been investigated through parameter variation.

Modeling Approach

As in many of earlier works on direct simulations of liquid–solid suspensions with full resolution of the interfaces, we used the lattice-Boltzmann (LB) method[28,29] to solve for the flow of the interstitial liquid. The method has a uniform, cubic grid (grid spacing Δ) on which fictitious fluid particles move in a specific set of directions, and collide to mimic the behavior of an incompressible, viscous fluid. The specific LB scheme employed here is due to Somers[36]; also see Ref. 37. The no-slip condition at the spheres' surfaces was dealt with by means of an immersed boundary (or forcing) method.[30,31] In this method, the sphere surface is defined as a set of closely spaced points (the typical spacing between points is 0.7 Δ), not coinciding with lattice points. At these points the (interpolated) fluid velocity is forced to the local velocity of the solid surface according to a control algorithm. The local solid-surface velocity has a translational and rotational contribution. Adding up (discrete integration) per spherical particle of the forces needed to maintain no-slip provides us with the (opposite; action equals minus reaction) force the fluid exerts on the spherical particle. Similarly the hydrodynamic torque exerted on the particles can be determined. Forces and torques are subsequently used to update the linear and rotational equations of motion of each spherical particle.

We have validated and subsequently used this method extensively to study the interaction of (static as well as moving) solid particles and Newtonian and non-Newtonian fluids. For instance, simulation results of a single sphere sedimenting in a closed container were compared with PIV experiments of the same system and showed good agreement in terms of the sphere's trajectory, as well as the flow field induced by the motion of the falling sphere for (at least) $Re \leq 30$.[38] For dense suspensions (with volume-averaged solids volume fractions up to 0.53) Derksen and Sundaresan[35] were able to quantitatively correctly represent the onset and propagation of instabilities (planar waves and two-dimensional voids) of liquid–solid fluidization as experimentally observed by Duru, Guazelli, and coworkers.[39,40]

It should be noted that having a spherical particle on a cubic grid requires a calibration step, as earlier realized by Ladd.[41] He introduced the concept of a hydrodynamic radius. The calibration involves placing a sphere with a given radius a_g in a fully periodic cubic domain in creeping flow and (computationally) measuring its drag force. The hydrodynamic radius a of that sphere is the radius for which the measured drag force corresponds to the expression for the drag force on a simple cubic array of spheres due to Ref. 42 which is a modification of the analytical expression due to Hasimoto.[43] Usually a is slightly bigger than a_g with $a - a_g$ typically equal to half a lattice spacing or less.

In previous articles,[35,38,44,45] we have repeatedly checked the impact of spatial resolution on the results of our simulations and we consistently concluded that a resolution such that a corresponds to six lattice spacing's is sufficient for accurate results (based on comparison with higher resolution simulations and with experimental data) as long as particle-based Reynolds numbers do not exceed values of the order of 50. The simulations presented in this article all have a resolution such that $a = 6\Delta$. Once the spatial resolution is fixed, the temporal resolution of the LB simulations goes via the choice of the kinematic viscosity. In all simulations discussed here the viscous time scale $\frac{a^2}{v}$ corresponds to 7,200 time steps.

The fixed-grid simulations involving moderately dense suspensions as discussed here require explicit inclusion of subgrid lubrication forces.[46] The expression for the radial lubrication force on two equally sized solid spheres i and j having relative velocity $\Delta\mathbf{u_{ij}} \equiv \mathbf{u_{pj}} - \mathbf{u_{pi}}$ reads[47]

$$F_{lub} = \frac{3}{2}\pi\rho v a^2 \frac{1}{s}\left(\mathbf{n}\cdot\Delta\mathbf{u}_{\mathbf{ij}}\right), \quad \mathbf{F_{lub,j}} = -F_{lub}\mathbf{n}, \quad \mathbf{F_{lub,i}} = F_{lub}\mathbf{n} \quad (5)$$

with s the smallest distance between the sphere surfaces $s \equiv |\mathbf{x_{pj}} - \mathbf{x_{pi}}| - 2a$, and (again, see before) $\mathbf{n}$ the unit vector pointing from the center of sphere i to the center of sphere j. Note that Eq. 5 is based on a creeping flow assumption in the (narrow) space between closely spaced spheres undergoing relative motion and, thus, valid for $\mathrm{Re}_s \equiv \frac{s|\Delta\mathbf{u_{ij}}|}{v} \ll 1$. Tangential lubrication forces and torques have not been considered since they are much weaker than the radial lubrication force; the former scale with $\ln\left(\frac{a}{s}\right)$, the latter (see Eq. 5) with $\frac{a}{s}$. The expressions in Eq. 5 need to be tailored for use in lattice-Boltzmann simulations[46]: (1) The lubrication force needs to be switched off when sphere surfaces are sufficiently separated in which case the LBM can accurately account for the hydrodynamic interaction between the spheres (typically if $s > \Delta$). (2) the lubrication force needs to saturate when solid surfaces are very close to account for surface roughness and to avoid very high levels of the lubrication force that could lead to unphysical instabilities in the simulations.[35]

A smooth way to turn on and off the lubrication force has been proposed in Ref. 46; instead of Eq. 5 one writes

$$F_{lub} = \frac{3}{2}\pi\rho v a^2\left(\frac{1}{s} - \frac{1}{s_0}\right)\left(\mathbf{n}\cdot\Delta\mathbf{u_{ij}}\right) \text{ if } s \leq s_0, \quad \text{and } F_{lub} = 0 \text{ if } s > s_0 \quad (6)$$

with the modeling parameter s_0 as the distance between solid surfaces below which the lubrication force becomes active. A second modeling parameter (s_1) is the distance below which the lubrication force gets saturated $F_{lub} = \frac{3}{2}\pi\rho v a^2\left(\frac{1}{s_1} - \frac{1}{s_o}\right)\left(\mathbf{n}\cdot\Delta\mathbf{u_{ij}}\right)$ if $s \leq s_1$. The settings for the lubrication force modeling parameters were $s_0 = 0.2a$ and $s_1 = 2{\cdot}10^{-4}a$. With this procedure and these settings accurate results

for close-range hydrodynamic sphere-sphere interactions have been reported.[35,46]

The spheres' equations of linear and rotational motion including resolved and unresolved (i.e., lubrication) forces are integrated according to an Euler forward method. These time-step driven updates are linked with an event-driven algorithm that detects events related to the SqWP and to hard-sphere collisions during the Euler time steps. Three types of events are being considered (1) a hard-sphere collision, (2) two approaching spheres enter one another's SqWP, and (3) two spheres that move apart reach a center-to-center distance of $2(a + \delta)$, and attempt to leave one another's SqWP. Event (3) has two possible outcomes: the spheres detach (if their relative velocity is sufficiently high), or do not detach. Once an event is being detected, all particles are frozen and the event is carried out which for all three event types implies an update of the linear velocities (and also angular velocities for event type (1) if $\mu \neq 0$) of the two spheres involved in the event. Subsequently, all spheres continue moving until the end of the time step, or until the next event.

Results

Verifications and preliminary simulations

In order to verify the simulation procedure and specifically the implementation of the SqWP, a number of granular simulations were performed. In a granular simulation a collection of spheres moves through vacuum. A sphere only changes velocity if it gets involved in one of the three events as identified in the previous section. The granular simulations are fully event-driven; for monitoring purposes, however, information regarding the system is stored at regular time intervals.

The results shown in Figure 1 are for 128 granularly moving spheres in a fully periodic, 3-D, cubic domain. The size of the domain is such that $\phi = 0.055$. In the initial state the spheres are randomly placed in the domain such that none of the spheres is attached to another sphere which implies that the system initially has the maximum possible potential energy. The spheres are given random velocities: each velocity component of each sphere is sampled from a uniform distribution in the interval $[-0.5u_0, 0.5u_0]$. The top panel of Figure 1 shows time series of the kinetic, potential, and total energy if the restitution coefficient $e = 1.0$, and friction coefficient $\mu = 0.0$. We see that total energy is conserved (with accuracy comparable to machine accuracy), and that the system reaches a stationary state approximately $300\frac{a}{u_0}$ after startup. If the restitution coefficient is reduced to $e = 0.999$ the system loses energy and eventually (after an elapsed time of $5000\frac{a}{u_0}$) comes to rest in the form of a single, large aggregate (see the bottom panel of Figure 1).

In a second preliminary simulation fluid is added to the system. To visualize the dynamics of aggregation and breakage and its interaction with liquid flow, the liquid–solid suspension is sheared by moving two parallel plates in opposite direction with $\mathrm{Re} = \frac{a^2\dot{\gamma}}{\nu} = 0.24$. Periodic boundary conditions apply in the streamwise (x), and transverse (y) direction. To clearly see all spheres and to identify attachment of spheres, the spheres centers are initially given equal y-coordinates and are not allowed moving in the y-direction. The size of the flow domain in y-direction is $4a$. The simulations are started from rest (liquid and solid have zero velocity), and initially none of the spheres is attached to another sphere.

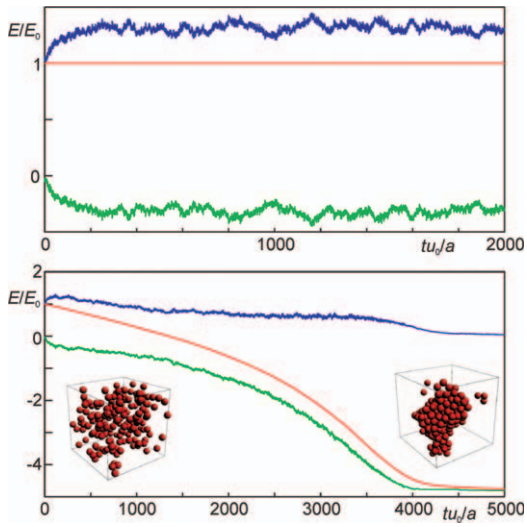

Figure 1. Energy time series E (normalized by initial energy E_0) of granular simulations.

128 solids spheres in a fully periodic cubic domain with size $L=21.3a$. Initial conditions: each velocity component of each sphere is a random number with uniform distribution in the interval $[-0.5u_0, 0.5u_0]$; spheres are randomly placed and are not attached. The square-well potential has $\frac{\delta}{a} = 0.05$ and $\frac{\Delta u}{u_0} = 0.4$. Top panel $e = 1.0$, bottom panel $e = 0.999$; Blue: kinetic energy; green: potential energy; red: total energy. The insets in the bottom panel are at $\frac{tu_0}{a} = 500$ and 5,000, respectively. [Color figure can be viewed in the online issue, which is available at wiley onlinelibrary.com.]

In Figure 2 it is shown how the flow develops in time, and that aggregates are formed and broken. Figure 3 shows a time series of the average number of sphere-sphere contacts per sphere; it illustrates that the system reaches a (dynamic) stationary state, with continuous attachment and detachment of spheres.

Aggregation in HIT

We now turn to suspensions in homogeneous, isotropic turbulence. Two base-cases were defined that only differ with regards to the friction coefficient μ: one base-case has $\mu = 0$, the other $\mu \to \infty$. Next to friction and the fixed settings as discussed previously, the physical dimensionless numbers were: solids-volume fraction $\phi = 0.080$, the Kolmogorov length scale over particle radius $\frac{\eta_K}{a} = 0.125$ with η_K based on the input value of the energy dissipation rate in the linear forcing scheme, and the dimensionless depth of the square well $\frac{\Delta u}{v} = 0.30$. For easy reference, Table 1 summarizes the dimensionless settings (except for $\frac{L}{a}$, see later) for the two base-cases.

An important question is how large the (cubic) domain needs to be to get representative results that are independent of the domain size. This is particularly relevant since our solid–liquid systems undergo aggregation and not only the primary sphere size should be much smaller than the domain size, also the aggregate size should be (much) smaller than the size of the domain to avoid the unphysical situation that an aggregate strongly interacts with itself through the periodic boundaries. Apart from aggregation and self-interaction between aggregates, the turbulence imposes demands on the domain size: it should have sufficient room to develop its wide spectrum of length scales to be representative for the strong turbulence in large-scale process equipment. Obviously, the

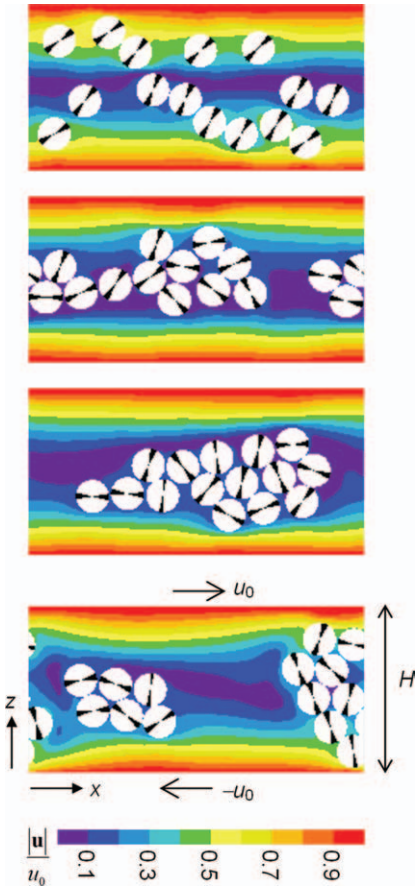

Figure 2. Sticky spherical particles in the shear flow generated by two flat parallel plates moving in opposite direction $\dot{\gamma} = \frac{2u_0}{H}$.

From top to bottom: snapshots at $t\dot{\gamma} = 2, 40, 80, 120$ after startup from rest. Periodic conditions apply in x and y direction; the spheres are not allowed to move in y-direction $\mathrm{Re} = \frac{a^2\dot{\gamma}}{\nu} = 0.24$; $e = 1.0$; $\frac{\delta}{a} = 0.05$; $\frac{\Delta u}{a\dot{\gamma}} = 0.25$; $\frac{H}{a} = 10.0$. The colors indicate fluid velocity magnitude. Cross section through the center of the channel; the width of the channel in y-direction is $4a$. [Color figure can be viewed in the online issue, which is available at wileyonlinelibrary.com.]

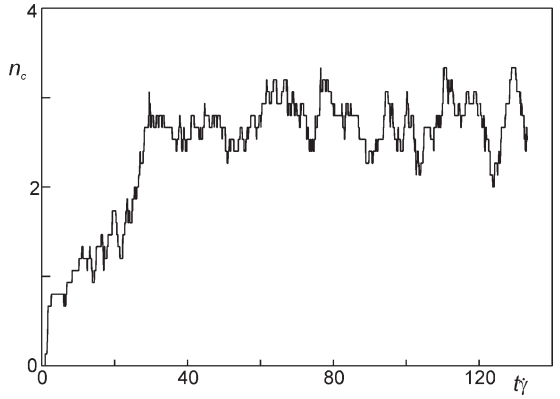

Figure 3. Situation as defined in Figure 2.

Time series of the average number of sphere-sphere contacts per sphere.

domain size is limited by the finite computational resources (time and memory) available. To investigate domain size effects, each of the two physical systems identified in Table 1 was simulated in cubic domains with four different vertex lengths: $L = 128 = 21.3a$, $L = 192 = 32a$, $L = 256 = 42.7a$, $L = 384 = 64a$ (as indicated earlier, the sphere radius a has not been varied and corresponds to six lattice spacing's).

All simulations reported here were run in sequential (single-cpu) mode. The computational effort obviously strongly depends on the system size. The largest simulations (with $L = 64a$) have $384^3 \approx 5.66 \cdot 10^7$ LB cells and contain almost 5,000 spheres. They take up approximately 11 Gbyte of memory. Completing one viscous time unit $\frac{a^2}{\nu}$ takes about 2 weeks on an Opteron 8431 (2.4 GHz) processor. The simulations scale almost perfectly with the grid size so that the corresponding case with $L = 128$ completes one viscous time unit in half a day.

To start with, we present results as to how the turbulently agitated suspensions evolve to a stationary state in Figure 4. The initial condition is a liquid velocity field $\mathbf{u} \equiv (u_x, u_y, u_z)$ that sinusoidally varies in space $u_x = u_0 \sin(2\pi y/\lambda_0)$, $u_y = u_0 \sin(2\pi z/\lambda_0)$, $u_z = u_0 \sin(2\pi x/\lambda_0)$ (to start a simulation a non-zero velocity field is required since the turbulence forcing is proportional to the fluid velocity); we set $\mathrm{Re}_0 \equiv \frac{u_0 a}{\nu} = 48$. If we slightly offset the wavelength from L divided by an integer number (typically $\lambda_0 = 1.01\frac{L}{4}$) the system quickly generates turbulence. This form of initial condition was chosen as it is a simple way to guarantee an initially divergence free velocity field. If the fluid flow is initialized such that $\nabla \cdot \mathbf{u} \neq 0$, the weakly compressible lattice-Boltzmann method in combination with linear forcing develops (initially very weak) density waves that slowly but steadily grow with time. This is unwanted given the long runs we need to first reach steady-state turbulence and steady ASD's and, subsequently, to obtain converged flow and particle statistics. The solids are randomly released in the cubic domain such that none of the spheres is attached to another sphere, and initially have zero velocity. Given the large computer runtime for the largest domain ($L = 384$), their time series are shorter than for the other simulations. They are, however, long enough for reaching a stationary state.

Since in the larger flow domains the turbulence is allowed to generate larger structures, the time to steady state (as measured in viscous time units $\frac{a^2}{\nu}$) gets longer for larger L (see Figure 4). Three variables have been tracked in Figure 4: the ratio $\frac{\eta_K}{a}$ (with now based on the actual dissipation in the liquid phase only—this needs to be stated explicitly since the immersed boundary method that we use to impose no-slip at sphere surfaces implies fictitious fluid inside the solids; the dissipation in this fluid is not considered when η_K is determined); the number of attachment points per sphere (n_c) as a metric for the level of aggregation; and a turbulence Reynolds

Table 1. Base-case Input Settings; Bold Face: Variables Fixed Throughout this Paper; Normal Print: Variables that have been Varied Later in this Article

Base-case #	$\frac{\rho_p}{\rho}$	ϕ	$\frac{\eta_K}{a}$	$\frac{\delta}{a}$	$\frac{\Delta u}{v}$	e	μ	$\frac{s_0}{a}$	$\frac{s_1}{a}$
1	**4.0**	0.08	0.125	**0.05**	0.30	**1.0**	0	**0.2**	$\mathbf{2 \cdot 10^{-4}}$
2	**4.0**	0.08	0.125	**0.05**	0.30	**1.0**	∞	**0.2**	$\mathbf{2 \cdot 10^{-4}}$

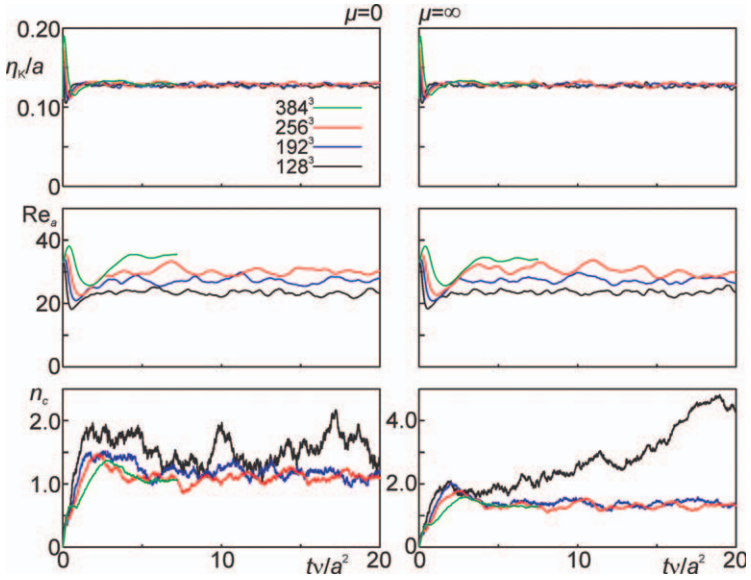

Figure 4. Time series of key variables of aggregating spheres in homogeneous isotropic turbulence.

From top to bottom: Kolmogorov length scale over particle radius, particle-size-based Reynolds number $\mathrm{Re}_a \equiv \frac{u_{rms}a}{\nu}$, number of sphere-sphere contacts per sphere. Left: frictionless collisions ($\mu = 0$), right: $\mu \to 0$. The colors indicate domain size. [Color figure can be viewed in the online issue, which is available at wileyonlinelibrary.com.]

number based on the volume-average root-mean-square velocity in the liquid and the primary sphere radius $\mathrm{Re}_a \equiv \frac{u_{rms}a}{\nu}$. The Taylor microscale λ_T in case of HIT is [32] $\lambda_T = \left(\frac{15\nu u_{rms}^2}{\varepsilon}\right)^{1/2}$. For our base-case situations $\lambda_T \approx 1.8a$ so that $\mathrm{Re}_T \equiv \frac{u_{rms}\lambda_T}{\nu} \approx 1.8\mathrm{Re}_a$.

The stable time series (after reaching steady state) of the ratio $\frac{\eta_K}{a}$, and the good agreement between its preset and actual values (preset 0.125, time-averaged actual 0.129) shows that the linear forcing procedure is able to maintain a constant, desired dissipation rate; also in the presence of solids. The dissipation rate is independent of the size of the computational domain, which it should be.

The steady state level of Re_a does depend on domain size L; if the domain gets larger, Re_a gets larger which means that the turbulent kinetic energy (TKE) per unit fluid mass increases. This is due to the larger, energy containing structures that fit in the larger domains. To quantify this, turbulent kinetic energy spectra are shown in Figure 5. The spectra for different domain sizes more or less overlap for the higher wave numbers $\kappa = \frac{2\pi}{\lambda}$. This is because the simulations with different domain sizes have the same dissipation rate and, therefore, develop the same small-scale turbulence. If we discard the simulations in the smallest domain ($L = 128$) the spectra only deviate significantly for the smaller wave numbers with $^{10}\log(\kappa a) < -0.5$, i.e., for flow structures with sizes larger than $\frac{2\pi a}{10^{-0.5}} \approx 20a$. As a result of this, the turbulent environment of the primary particles and also of small aggregates can be considered (statistically) similar for the simulations at different domain size, as long as $L \geq 192$. This is likely the reason why the average number of contacts per sphere (bottom panels of Figure 4) is approximately independent of the domain size, again as long as $L \geq 192$.

For the smallest simulations ($L = 128$), the number of contacts per sphere is clearly different, and also the spectra deviate over larger portions of the wave number space (Figure 5), and we conclude that such a domain is too small. In the case with $\mu \to \infty$ a stationary state is actually not reached if $L = 128$; the number of contacts per sphere keeps increasing. Closer inspection reveals that the spheres keep on aggregating and tend to form a single, big aggregate. If (for $L \geq 192$) steady-state n_c values are compared between $\mu = 0$ and $\mu \to \infty$, friction induces higher levels of attachment of spheres and, thus, probably larger aggregates. Aggregate size distributions will be discussed in the next subsection.

The bottom panel of Figure 5 shows a comparison between a single-phase (liquid only) spectrum, and solid–liquid spectra (the latter are the same data as in the top panels for $L = 256$): The presence of solids enhances TKE for high-wave numbers at the expense of TKE for lower wave numbers which is a known effect that has been reported in earlier computational studies.[32,33]

Aggregates: size distribution and structure

We now turn to the structure and size of the aggregates that are continuously formed and broken as a result of the turbulent flow. In Figure 6 instantaneous realizations of particle configurations are given. From the panel related to $L = 128$ it may be more clear that—as argued previously—this domain is too small for a domain-size-independent representation of the turbulence-aggregation interaction; larger domains are clearly needed. The bottom panels of Figure 6 show the largest aggregates at a certain (arbitrary) moment in time, suggesting larger aggregates when collisions between primary spheres are frictional. They also suggest a fairly open aggregate structure, i.e., relatively low-fractal dimensions. An impression of the flow field the particles move in is given in Figure 7. The main purpose of Figure 7 is to show that the size of the smaller flow structures is comparable to the size of the primary particles as should be since $\frac{\eta_K}{a} < 1$. Van Vliet et al.[48] suggest that if a flow is visualized in a way similar as in Figure 7, the smallest scales that show up have a size of the order of 10 η_K.

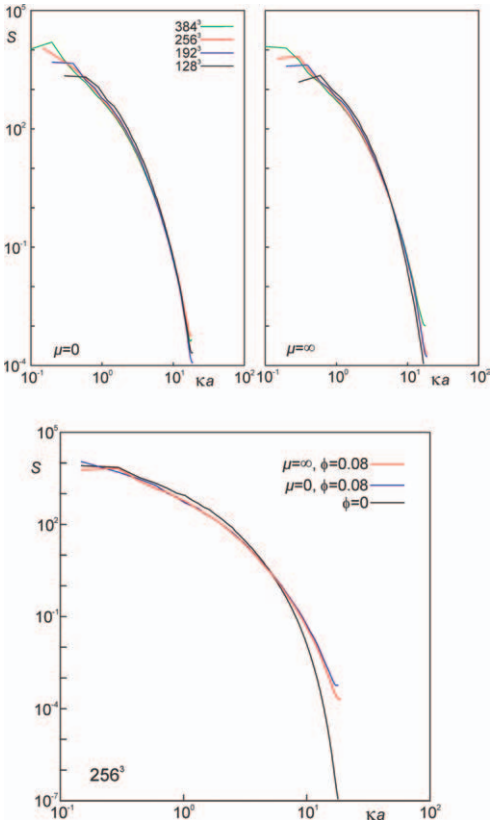

Figure 5. Power spectral density of turbulent kinetic energy as a function of dimensionless wave number κa after steady state has been reached.

Top: the same solid–liquid systems as in Figure 4. Bottom: comparison between a single-phase spectrum ($\phi = 0$) with the solid–liquid spectra for $L = 256$. [Color figure can be viewed in the online issue, which is available at wileyonlinelibrary.com.]

To make the observations in Figure 6 regarding the aggregates more quantitative and also to further investigate domain-size effects, time-averaged ASD's were determined. The ASD's presented in this article are by aggregate mass (which is the same as by aggregate volume or by aggregate size in terms of the number of primary spheres n_{agg} given the monodisperse primary spheres). To determine ASD's we took a large number of instantaneous realizations during the stationary portion ($t \geq 5\frac{a^2}{\nu}$) of the time series shown in Figure 4 (except for the case with $L = 128$ and $\mu \to \infty$ that did not become steady; for this case we also started building an ASD from $t = 5\frac{a^2}{\nu}$ on). The size distributions for the same cases for which we showed the time series in Figure 4 are given in Figure 8. For $\mu = 0$ the ASD is fairly independent of L as long as $L \geq 192$; the case with $L = 128$ deviates strongly. The mass-averaged aggregate sizes are $\langle n_{agg} \rangle = 2.60, 2.07, 1.97, 1.88$ for $L = 128, 192, 256, 384$, respectively, which (beyond $L = 128$) shows a weak trend toward smaller $\langle n_{agg} \rangle$ for larger domains. This may be due to the stronger turbulence (albeit at the larger scales only) for the larger domains. Also for $\mu \to \infty$ ASD's are similar if $L \geq 192$. The average aggregate sizes are (in the order small to large domain) 4.63, 2.42, 2.27, and 2.22, i.e., slightly but significantly larger than for $\mu = 0$.

Based on what was learned previously, a number of simulations were performed all having $L = 256$ and $\mu \to \infty$. The settings for $\frac{\eta_K}{a}$, ϕ, and $\frac{\Delta u}{\upsilon}$ were varied: we took the base-case conditions (Table 1) and one-by-one increased and decreased each of these three dimensionless numbers (total of six additional simulations). Note that changing one dimensionless number and keeping the rest the same sometimes implies changing more than one physical parameter. For instance, a decrease in the ratio $\frac{\eta_K}{a}$ was achieved by increasing the energy dissipation rate, thus, reducing the Kolmogorov length scale. At the same time the Kolmogorov velocity scale υ increases. In order to keep $\frac{\Delta u}{\upsilon}$ constant, we increase $\Delta\upsilon$ (and thus the binding energy) by the same factor as υ increases.

The resulting ASD's are presented in Figure 9. A striking observation is that the aggregating solid–liquid systems can quickly get unstable, i.e., do not reach a dynamically stationary ASD. If the depth of the square well $\frac{\Delta u}{\upsilon}$ is increased from 0.30 to 0.35 (an increase by a factor of 1.36 in the binding energy which is proportional to $(\Delta u)^2$) the system slowly but consistently keeps on aggregating without reaching a steady ASD; see the lower panel of Figure 9 and its inset. If the solids volume fraction is increased from $\phi = 0.08$ (base-case) to 0.16 a large aggregate consisting of the order of 2,000 primary spheres is formed (the total number of primary spheres in this simulation is 2,960), surrounded by a number of smaller aggregates and primary spheres; see the middle panel of Figure 9 plus inset.

Apart from the unstable nature of some of the aggregating solid–liquid systems, the results in terms of ASD's follow expected trends: For a given primary particle size, a decrease in $\frac{\eta_K}{a}$ means a decrease in the Kolmogorov length scale as a result of an increasing energy dissipation rate. Since (unless stated otherwise) the ASD's were obtained during a stationary time window, dissipation is in equilibrium with power input, and higher dissipation implies higher power input and, thus, stronger turbulence. The results in the top panel of Figure 9, therefore, show a shift toward smaller aggregate sizes if the power input is increased. Starting at the highest value of $\frac{\eta_K}{a}$, from one case to the next the power input increases by a factor of 4. For $\frac{\eta_K}{a} = 0.181, 0.129, 0.091$, the respective mass-average aggregate sizes $\langle n_{agg} \rangle$ are 3.99, 2.27, and 1.71. The average aggregate size is approximately linear in $\frac{\eta_K}{a}$ in the (fairly narrow) range considered here.

In the aforementioned discussion the denser suspensions ($\phi = 0.16$) we investigated became unstable. The more dilute suspension with $\phi = 0.04$ develops much smaller aggregates compared to the base-case, largely because collisions are much less frequent in the dilute suspension (middle panel of Figure 9). Also the influence of the depth of the square-well follows our intuition: the shallower interaction potential leads to smaller aggregates; the deeper well to larger aggregates (bottom panel of Figure 9).

Next to aggregate size, aggregate structure has been investigated. A frequently used metric for this is the fractal dimension (symbol d_f) of aggregates (e.g., Ref. 6). Fractal dimensions span the range from one (needle and fiber-shaped aggregates) to three (compact, near-spherically shaped aggregates). The experimental and computational literature dealing with structuring of aggregates in laminar flows and turbulent flows such that $\frac{\eta_K}{a} \gg 1$ indicates a dependency of the fractal dimension on the deformation

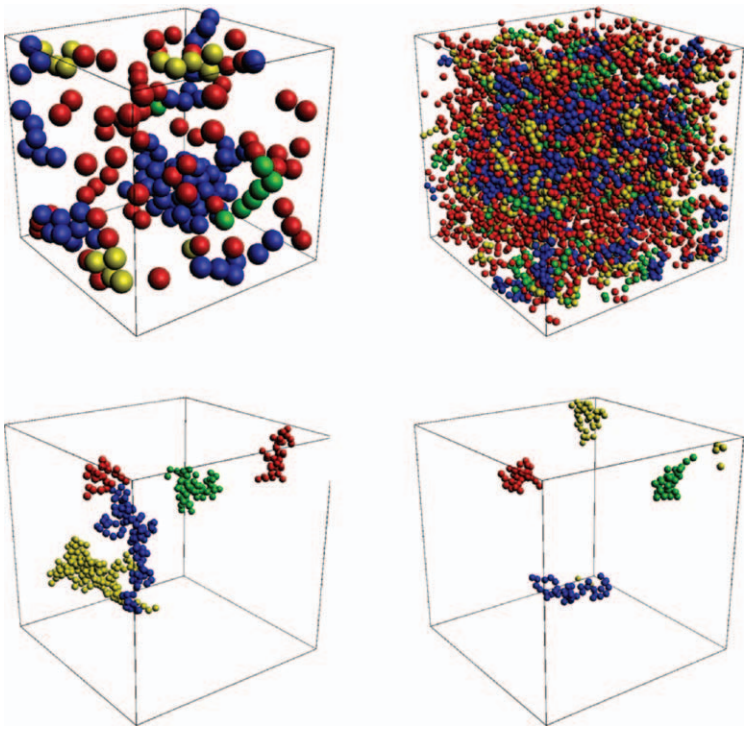

Figure 6. Single realizations of aggregates in cubic domains.

Top: primary spheres colored by the size of the aggregate they are part of (red: $n_{agg} < 4$; yellow: $4 \leq n_{agg} < 7$; green: $7 \leq n_{agg} < 10$; blue: $n_{agg} \geq 10$). Top-left: $L = 128$; top-right $L = 384$. Base-case with $\mu \to \infty$. Bottom: the four biggest aggregates for base-cases with $L = 384$; left $\mu \to \infty$ (red $n_{agg} = 60$, yellow $n_{agg} = 150$, green $n_{agg} = 65$, blue $n_{agg} = 105$, and the red aggregate connects through the periodic boundaries); right $\mu = 0$ (red: $n_{agg} = 32$, yellow: $n_{agg} = 46$, green $n_{agg} = 31$, blue: $n_{agg} = 41$; the yellow aggregate connects through the periodic boundaries). [Color figure can be viewed in the online issue, which is available at wileyonlinelibrary.com.]

levels and flow topology experienced by the aggregates (e.g., Ref. 23).

A commonly used way of determining the fractal dimension of an ensemble of aggregates goes via their radius of gyration.[6] Since our aggregates consist of identical spherical particles, R_g can be determined according to $\boldsymbol{R_g^2} = \frac{1}{n_{agg}} \sum_{i=1}^{n_{agg}} |\mathbf{x_i} - \mathbf{x_c}|^2$, with n_{agg} the number of primary spheres in the aggregate, $\mathbf{x_i}$ the center position of primary sphere i, and the center of gravity of the aggregate $\mathbf{x_c} = \frac{1}{n_{agg}} \sum_{i=1}^{n_{agg}} \mathbf{x_i}$. The aggregate size n_{agg} and its radius of gyration scale according to $n_{agg} \propto R_g^{df}$. For determining the fractal dimension of an ensemble of aggregates the standard procedure is to double-logarithmically plot aggregate size vs. radius of gyration (in an experiment they can be measured independently,[23] in a simulation they are directly available), and fit a straight line through the data points. The slope of the line is d_f. To be consistent with the literature, the same procedure is followed here. It should be noted, however, that applying the procedure requires making a few choices. Their impact on the outcome (d_f) is discussed later. Only simulations with $L = 256$ have been analyzed in terms of d_f.

In Figure 10, $\frac{R_g}{a}$ is plotted vs. n_{agg} for one specific simulation (base case with $\mu \to \infty$, see Table 1). Each dot in the figure represents an aggregate as observed in snapshots taken under steady-state conditions in a time interval with length $15\frac{a^2}{\nu}$. The total number of dots in Figure 10 is approximately 56,000. The discrete nature of the aggregates is clear from the horizontal bands in Figure 10 that relate to the smaller aggregates. The wide extent of the cloud of points, and the many smaller than larger aggregates, make it not straightforward to unambiguously fit a linear function. Next to the great many dots, Figure 10 contains six linear function fits. The three solid lines represent fits according to $n_{agg} = \alpha\left(\frac{R_g}{a}\right)^{d_f}$ with two degrees-of-freedom (DoF's) α and d_f per fit. Each solid line relates to a different minimum aggregate size the fit is based on. The black line is based on all aggregates ($n_{agg} \geq 2$), the blue and red solid lines are based on $n_{agg} \geq 4$ and $n_{agg} \geq 16$, respectively. This was done to assess the effect of the small aggregates on the outcome of the fitting process. The slopes and, thus, fractal dimensions based on these fits are 1.53, 1.63, and 1.30, respectively. The fit for $n_{agg} \geq 16$ clearly deviates from the other two, and so does its intercept with the ordinate (α). In the literature[6] the following correlation for α has been suggested $\alpha = 4.5 d_f^{-2.1}$. The α's of the fits with $n_{agg} \geq 2$ ($\alpha = 1.87$), and $n_{agg} \geq 16$ ($\alpha = 1.76$) are well in line with this correlation; the fit for $n_{agg} \geq 16$ ($\alpha = 3.72$) not, and we dismiss the latter fit.

The dashed lines in Figure 10 only have d_f as the fitting parameter. In these one-DoF fits we require the linear function to go through the *a priori* known average radius of gyration of a sphere doublet; for $n_{agg} = 2 : \frac{R_g}{a} = 1 + \frac{\delta}{\sqrt{3}a}$. The colors of the dashed lines relate to the minimum aggregate size involved in the fit in the same way as the colors of the solid lines. The fractal dimensions for the one-DoF fits are

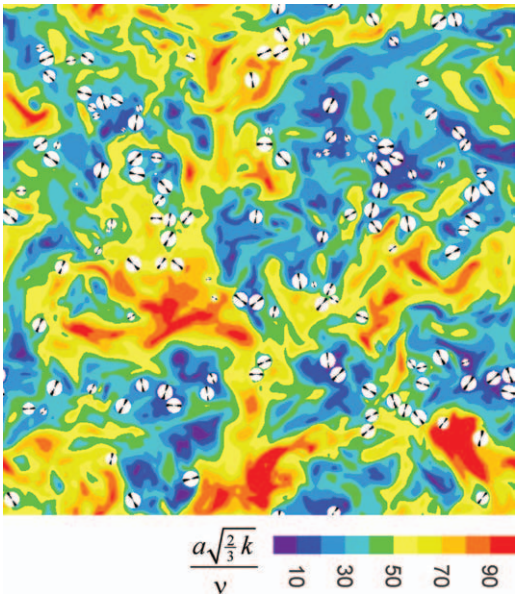

Figure 7. Cross section through the base-case flow with $\mu \to \infty$ and $L = 384$.

The black-white discs are cross sections of the primary spheres; the colors indicate nondimensional instantaneous velocity magnitudes ($\sqrt{\frac{2}{3}k}$). [Color figure can be viewed in the online issue, which is available at wileyonlinelibrary.com.]

1.49, 1.53, and 1.64. The five fits (the sixth was dismissed, see before) have average $d_f = 1.56$ and standard deviation 0.07. We propose $d_f = 1.56 \pm 0.07$.

Given the wide extent of the cloud of points in the R_g *vs* n_{agg} plots and the related ambiguity in fitting d_f, the fractal dimension may not be the best way to quantify aggregate structure as encountered in our simulations. However, since d_f is a widely used quantity in the literature, we analyzed all of our simulations with domain size $L = 256$ in terms of fractal dimension. Our earlier observations regarding the fitting procedure led us to base fractal dimensions on one-DoF fits for aggregates with sizes larger or equal than four primary spheres ($n_{agg} \geq 4$). We estimate the uncertainty in d_f to be of order 0.1.

The fractal dimensions are given in Table 2. According to these results, the turbulent flow is unable to make dense aggregates; d_f hardly exceeds 1.7 and gets as low as 1.4.

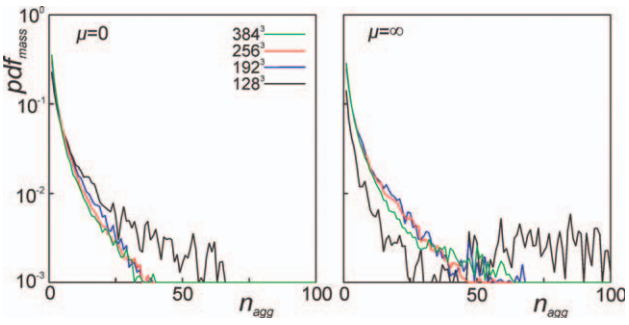

Figure 8. Aggregate size distributions by mass for the cases defined in Figure 4.

Comparison between frictionless (left) and frictional (right) collisions, and effects of system size. [Color figure can be viewed in the online issue, which is available at wileyonlinelibrary.com.]

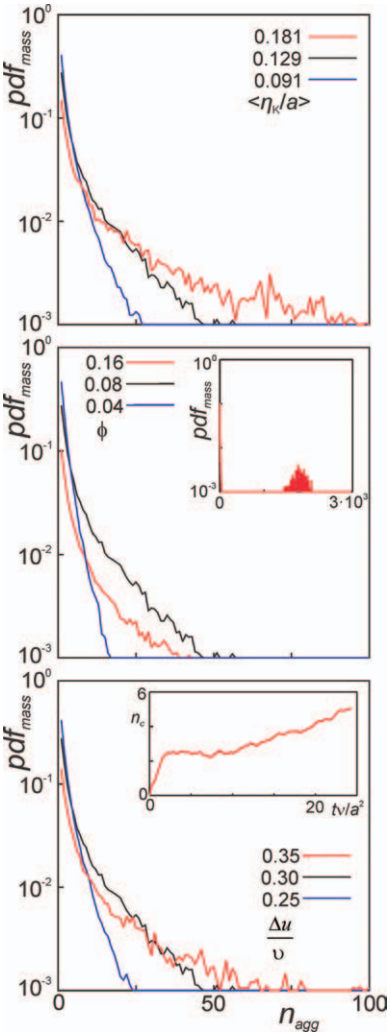

Figure 9. ASD's by mass for $L = 256$ domains, averaged over the time-interval $5 \leq \frac{tv}{a^2} < 20$; effects of physical settings.

From top to bottom: effect of $\frac{\eta_K}{a}$; solids volume fraction ϕ (the inset has an extended abscissa to show the large aggregates for $\phi = 0.16$); (the inset shows the number of contacts per sphere as a function of time for $\frac{\Delta_u}{v} = 0.35$ to indicate its nonstationary behavior in the averaging time-window). [Color figure can be viewed in the online issue, which is available at wileyonlinelibrary.com.]

Such values for fractal dimension are typical for diffusion-limited aggregation,[49] not so much for aggregation in turbulent flows.[50] We speculate that this seeming paradox is a consequence of the primary spheres being larger than the Kolmogorov scale. The common condition for making dense aggregates in turbulent flow is that $\frac{\eta_K}{a} \gg 1$, not $\frac{\eta_K}{a} = O(0.1)$ as is the case here. If $\frac{\eta_K}{a} \gg 1$ the fluid deformation experienced by the primary particles and aggregates is homogeneous (albeit time-dependent). This is fundamentally different from the inhomogeneous, turbulent (and thus erratic) flow experienced by the solids if $\frac{\eta_K}{a} = O(0.1)$. Given the results for fractal dimension (Table 2), the erratic nature of the flow at the scale of the aggregates brings about aggregation akin to a diffusive process. The fractal dimension increasing if $\frac{\eta_K}{a}$ gets larger tentatively supports this view as an increase of $\frac{\eta_K}{a}$ moves us closer to the more common situation with $\frac{\eta_K}{a} \gg 1$.

The other dependencies in Table 1 (slightly compacter aggregates for a stronger square-well potential and for a

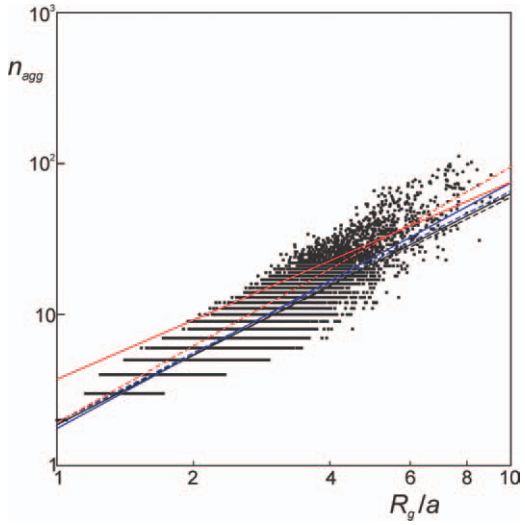

Figure 10. Radius of gyration $\frac{R_g}{a}$ vs. aggregate size.

Base case with $\mu \to \infty$. Dots: individual aggregates. Lines: fits with $n_{agg} \propto R_g^{d_f}$ with d_f the fractal dimension. Solid lines: fits with two degrees-of-freedom; dashed lines: fits with one degree-of-freedom (see text). Black lines: fit for all aggregates; blue: fit only for $n_{agg} \geq 4$; red: fit only for $n_{agg} \geq 16$s. [Color figure can be viewed in the online issue, which is available at wileyonlinelibrary.com.]

higher solids volume fraction) were to be expected: stronger attraction between primary spheres makes more compact aggregates; with more solids in an isotropic flow there is less room to build and sustain long, slender aggregates.

Summary and Conclusions

In this article, we have presented detailed simulations of turbulent solid–liquid suspensions with the solids having a tendency to aggregate. The focus is on how turbulence interacts with the aggregation process. Turbulence plays a dual role: in the first place it promotes collisions that potentially lead to aggregation events, in the second place its fluid deformation induces disruptive forces on aggregates that can lead to breakage. At the same time, the presence of solids also couples back to the turbulence: the solid particles enhance small-scale turbulence, particularly in the moderately dense (solids volume fraction of the order of 10%) suspensions studied here. The systems considered are relatively simple: (1) the solid particles are spherical, and all have the same size, (2) the turbulence is homogeneous and isotropic and the flow domain is fully periodic, and (3) the interaction potential that is the reason for aggregation is a simple square-well potential.

In the simulations the solids and fluid phase are fully coupled, and the flow around the finite-size particles is resolved, except for when spheres are in very close proximity; then the resolved hydrodynamic forces on the spheres are supplemented with analytic expressions for radial lubrication forces. The turbulence is generated through linear forcing and is resolved down to the Kolmogorov scale. The square-well potential as aggregation mechanism was chosen for its simplicity. It only has two parameters and can be computationally efficiently combined with an event driven hard-sphere collision algorithm. We need the tight coupling between solid and fluid and the high level of detail including resolution of the flow around the particles since the Kolmogorov scale is of the same order of magnitude as the size of the primary particles and microturbulence, and the aggregation process have comparable and, therefore, interacting length scales.

The periodic flow domains need to be sufficiently large to develop a dynamically stationary aggregate size distribution. In investigating the impact of domain size we observed an increase in turbulent kinetic energy with increasing domain size. This was because the differently sized cases had the same turbulence microscale (same ε and ν). Since $\varepsilon \propto \frac{u_{rms}^3}{L}$, TKE $\propto u_{rms}^2 \propto (\varepsilon L)^{2/3}$, i.e., at constant dissipation rate larger domains are able to generate more kinetic energy and larger turbulent structures. What matters for the aggregation process, however, is the energy contained in the length scales up to the sizes of the aggregates, and we were able to generate aggregate size distribution that were fairly independent of the size of the flow domain, as long as $L \geq 32a$.

We clearly observed how stronger turbulence shifts aggregate-size distributions toward smaller aggregates, and how stronger interaction potentials make aggregates bigger. A fairly moderate increase in $\frac{\Delta u}{\upsilon}$ turned a stationary, stable aggregate size distribution unstable, generating a single, large aggregate with a size comparable to the size of the domain. A similar instability occurred when the solids volume fraction was increased. In addition to the square-well potential, spheres interact through hard-sphere collisions. The friction coefficient related to the hard-sphere collisions was shown to have influence on the aggregate size distribution.

The aggregate structures were quantified by their fractal dimensions d_f. To determine these, of large ensembles of aggregates, size n_{agg}, and radius of gyration R_g were determined, and the relationship $n_{agg} = \alpha\left(\frac{R_g}{a}\right)^{d_f}$ was fitted. This analysis showed quite wide scatter and related uncertainty in the fitting parameters α and d_f. Despite this uncertainty, it is clear that the aggregates have an open structure characterized by low-fractal dimension d_f hardly exceeded 1.7. We explain this by the erratic/diffusive nature of the particle motion in a turbulent field where particles are generally larger than the Kolmogorov scale.

Ehrl et al.[50] observed in their experiments (with $\frac{\eta_K}{a} \gg 1$) that the radius of gyration R_g scaled with the energy dissipation rate ε according to $R_g \propto \varepsilon^{-0.25}$. In our simulations (with $\frac{\eta_K}{a} = O(0.1)$) tentatively $n_{agg} \propto \eta_K \propto \varepsilon^{-0.25}$, so that $R_g \propto \varepsilon^{-0.25/df}$ which clearly is a different scaling than in the experiments,[50] since in our simulations $d_f \approx 1.4-1.7$. For this and additional reasons, the way d_f depends on $\frac{\eta_K}{a}$ deserves attention in future research. It is known that dense (high-dimensional) aggregates are formed in turbulent flow if $\frac{\eta_K}{a} \gg 1$. The open structure for relatively small $\frac{\eta_K}{a}$ ($O(0.1)$) as observed in this study, therefore, has to become denser upon increasing $\frac{\eta_K}{a}$. In order go toward (much) higher $\frac{\eta_K}{a}$ with simulation like the ones presented here, however, we need (much) larger flow domains. Resolution requirements dictate the sphere radius a to be typically six lattice spacing's, we, thus,

Table 2. Fractal Dimensions (d_f) of Aggregates as a Function of Flow Conditions and SqWP Parameters*

Main feature	μ	η_K/a	ϕ	$\Delta u/\upsilon$	$d_f \pm 0.1$
zero friction base-case	0	0.13	0.080	0.30	1.49
∞friction base-case	∞	**0.13**	**0.080**	**0.30**	**1.53**
stronger turbulence	∞	0.091	0.080	0.30	1.44
weaker turbulence	∞	0.18	0.080	0.30	1.66
more dilute suspension	∞	0.13	0.040	0.30	1.37
denser suspension	∞	0.13	0.16	0.30	1.71
weaker SqWP	∞	0.13	0.080	0.25	1.44
stronger SqWP	∞	0.13	0.080	0.35	1.67

*In addition to the given conditions the default settings apply. The system size is L=256 in all cases.

need to increase η_K. In order to have a sufficiently wide spectrum of turbulent length scales we then also have to increase the macroscopic turbulent scales, hence, consider larger flow domains. Larger domains are very well doable given that the simulations presented here are all sequential. Parallelization would lead the way to larger simulations. Note that some modeling/software challenges would need to be overcome in a parallel code, specifically related to its event- driven components.

Literature Cited

1. Hounslow MJ, Mumtaz HS, Collier AP, Barrick JP, Bramley ASA. Micro-mechanical model for the rate of aggregation during precipitation from solution. *Chem Eng Sci*. 2001;56:2543–2552.
2. Hollander ED, Derksen JJ, Portela LM, Van den Akker HEA. A numerical scale-up study for orthokinetic agglomeration in stirred vessels. *AIChE J*. 2001;47:2425–2440.
3. Guerrero-Sanchez C, Erdmenger T, Ereda P, Wouters D, Schubert US. Water-soluble ionic liquids as novel stabilizers in suspension polymerization reactions: Engineering polymer beads. *Chemistry A*. 2006;12:9036–9045.
4. Russel WB, Saville DA, Schowalter WR. *Colloidal Dispersions*. New York: Cambridge University Press; 1989.
5. Fitch B. Sedimentation of flocculent suspensions: state of the art. *AIChE J*. 1979;25:913–930.
6. Ehrl L, Soos M, Lattuada M. Generation and geometrical analysis of dense clusters with variable fractal dimension. *J Phys Chem B*. 2009;113:10587–10599.
7. Eggersdorfer ML, Kadau D, Herrmann HJ, Pratsinis SE. Fragmentation and restructuring of soft-agglomerates under shear. *J Colloid Interface Sc*. 2010;342:261–268.
8. Kwade A, Schwedes J. Breaking characteristics of different materials and their effect on stress intensity and stress number in stirred media mills. *Powder Tech*. 2002;122:109–121.
9. Ramkrishna, D. *Population balances - Theory and Applications to Particulate Systems in Engineering*. London: Academic Press; 2000.
10. Marchisio DL, Pikturna JT, Fox RO, Vigil D, Barresi AA. Quadrature method of moments for population balances. *AIChE J*. 2003;49:1266–1276.
11. Aamir E, Nagy ZK, Rielly CD, Kleinert T, Judat B. Combined quadrature method of moments and method of characteristics approach for efficient solution of population balance models for dynamic modeling and crystal size distribution control of crystallization processes. *Ind Eng Chem Res*. 2009;48:8575–8584.
12. Vigil RD. On equilibrium slutions of aggregation-fragmentation problems. *J Colloid Interface Sc*. 2009;336:642–647.
13. Soos M, Sefcik J, Morbidelli M. Investigation of aggregation, breakage and restructuring kinetics of colloidal dispersions in turbulent flows by population balance modeling and static light scattering. *Chem Eng Sci*. 2006;61:2349–2363.
14. Marchisio DL, Soos M, Sefcik J, Morbidelli, M. Role of turbulent shear rate distribution in aggregation and breakage processes. *AIChE J*. 2006;52:158–173.
15. Delichatsios MA, Probstein RF. The effect of coalescence on the average drop size in liquid-liquid dispersions. *Ind Eng Chem Fund*. 1976;14:134–138.
16. Kusters KA. The influence of Turbulence on Aggregation of Small Particles in Agitated Vessel. [Ph.D. Thesis]. Eindhoven University of Technology, Netherlands; 1991.
17. Derksen JJ, Eskin D. Potential of microchannel flow for agglomerate breakage. *Ind Eng Chem Res*. 2010;49:10633–10640
18. Bäbler MU, Morbidelli M, Bałdyga J. Modelling the breakup of solid aggregates in turbulent flows. *J Fluid Mech*. 2008;612:261–289.
19. Zaccone A, Soos M, Lattuada M, Wu H, Bäbler MU, Morbidelli M. Breakup of dense colloidal aggregates under hydrodynamic stresses. *Phys Rev E*. 2009;79:061401.
20. Soos M, Ehrl L, Bäbler MU, Morbidelli M. Aggregate breakup in a contracting nozzle. *Langmuir*. 2010;26:10–18.
21. Higashitani K, Iimura K, Sanda H. Simulation of deformation and breakup of large aggregates in flows of viscous fluids. *Chem Eng Sc*. 2001;56:2927–2938.
22. Becker V, Schlauch E, Behr M, Briesen H. Restructuring of colloidal aggregates in shear flows and limitations of the free-draining approximation. *J Colloid Interface Sc*. 2009;339:362–372.
23. Harshe YM, Lattuada M, Soos M. Experimental and modeling study of breakage and restructuring of open and dense colloidal aggregates. *Langmuir*. 2011;27:5739–5752.
24. Brady JF, Bossis G. Stokesian dynamics. *Annu Rev Fluid Mech*. 1988;20:111–157.
25. Harada S, Tanaka R, Nogami H, Sawada M. Dependence of fragmentation behavior of colloidal aggregates on their fractal structure. *J Colloid Interface Sci*. 2006;301:123–129.
26. Rosales C, Meneveau C. Linear forcing in numerical simulations of isotropic turbulence: Physical space implementations and convergence properties. *Phys Fluids* 2005;17:095106–1-8.
27. Smith SW, Hall CK, Freeman DB. Molecular dynamics for polymeric fluids using discontinuous potentials. *J Comp Phys*. 1997;134:16–30.
28. Chen S, Doolen GD. Lattice Boltzmann method for fluid flows. *Annu Rev Fluid Mech*. 1989;30:329–364.
29. Succi S. *The lattice Boltzmann equation for fluid dynamics and beyond*. Oxford: Clarendon Press; 2001.
30. Goldstein D, Handler R, Sirovich L. Modeling a no-slip flow boundary with an external force field. *J Comp Phys*. 1993;105:354–366.
31. Derksen J, Van den Akker HEA. Large-eddy simulations on the flow driven by a Rushton turbine. *AIChE J*. 1999;45:209–221.
32. Ten Cate A, Derksen JJ, Portela LM, Van den Akker HEA. Fully resolved simulations of colliding spheres in forced isotropic turbulence. *J Fluid Mech*. 2004;519:233–271.
33. Lucci F, Ferrante A, Elghobashi S. Modulation of isotropic turbulence by particles of Taylor length-scale size. *J Fluid Mech*. 2010;650:5–55.
34. Yamamoto Y, Potthoff M, Tanaka T, Kajishima T, Tsuji Y. Large-eddy simulation of turbulent gas-particle flow in a vertical channel: effect of considering inter-particle collisions. *J Fluid Mech*. 2001;442:303–334.
35. Derksen JJ, Sundaresan S. Direct numerical simulations of dense suspensions: wave instabilities in liquid-fluidized beds. *J Fluid Mech*. 2007;587:303–336.
36. Somers JA. Direct simulation of fluid flow with cellular automata and the lattice-Boltzmann equation. *Appl Sci Res*. 1993;51:127–133.
37. Eggels JGM, Somers JA. Numerical simulation of free convective flow using the lattice-Boltzmann scheme. *Int J Heat Fluid Flow*. 1995;16:357–364.
38. Ten Cate A, Nieuwstad CH, Derksen JJ, Van den Akker HEA. PIV experiments and lattice-Boltzmann simulations on a single sphere settling under gravity. *Phys Fluids*. 2002;14:4012–4025.
39. Duru P, Nicolas M, Hinch J, Guazelli E. Constitutive laws in liquid-fluidized beds. *J Fluid Mech*. 2002;452:371–404.
40. Duru P, Guazelli E. Experimental investigations on the secondary instability of liquid-fluidized beds and the formation of bubbles. *J Fluid Mech*. 2002;470:359–382.
41. Ladd AJC. Numerical simulations of particle suspensions via a discretized Boltzmann equation. Part I: Theoretical Foundation. *J Fluid Mech*. 1994;271:285–309.
42. Sangani AS, Acrivos A. Slow flow through a periodic array of spheres. *Int J Multiphase Flow*. 1982;8:343–360.
43. Hasimoto H. On the periodic fundamental solutions of the Stokes equations and their application to viscous flow past a cubic array of spheres. *J Fluid Mech*. 1959;5:317–328.
44. Derksen JJ. Flow induced forces in sphere doublets. *J Fluid Mech*. 2008;608:337–356.
45. Derksen JJ. Drag on random assemblies of spheres in shear-thinning and thixotropic liquids. *Phys Fluids*. 2009;21:083302–1-9.
46. Nguyen N-Q, Ladd AJC. Lubrication corrections for lattice-Boltzmann simulations of particle suspensions. *Phys Rev E*. 2002;66: 046708.
47. Kim S, Karrila SJ. *Microhydrodynamics: Principles and selected applications*. Boston: Butterworth-Heinemann; 1991.
48. Van Vliet E., Derksen JJ, Van den Akker HEA. Turbulent mixing in a tubular reactor: assessment of an FDF/LES approach. *AIChE J*. 2005;51:725–739.
49. Witten TA Jr, Sander LM. Diffusion-limited aggregation, a kinetic critical phenomenon. *Phys Rev Lett*. 1981;47:1400–1403.
50. Ehrl L, Soos M, Wu H, Morbidelli M. Effect of flow field heterogeneity in coagulators on aggregate size and structure. *AIChE J*. 2010;56:2573–2587.

Manuscript received May 11, 2011, and revision received Aug. 4, 2011.